

E. Havlickova, J. Harrison, B. Lipschultz, G. Fishpool, A. Kirk, A. Thornton,
M. Wischmeier, S. Elmore, S. Allan

SOLPS Analysis of the MAST-U Divertor with the Effect of Heating Power and Pumping on the Access to Detachment in the Super-X Configuration

Enquiries about copyright and reproduction should in the first instance be addressed to the Culham Publications Officer, Culham Centre for Fusion Energy (CCFE), Library, Culham Science Centre, Abingdon, Oxfordshire, OX14 3DB, UK. The United Kingdom Atomic Energy Authority is the copyright holder.

SOLPS Analysis of the MAST-U Divertor with the Effect of Heating Power and Pumping on the Access to Detachment in the Super-X Configuration

E. Havlickova¹, J. Harrison¹, B. Lipschultz², G. Fishpool¹, A. Kirk¹, A. Thornton¹,
M. Wischmeier³, S. Elmore¹, S. Allan¹

¹*Culham Centre for Fusion Energy, Culham Science Centre, Abingdon, OX14 3DB, United Kingdom*

²*Department of Physics, University of York, Heslington, York, YO10 5DD, United Kingdom*

³*Max-Planck Institut für Plasmaphysik, Boltzmannstraße 2, D-85748 Garching, Germany*

SOLPS analysis of the MAST-U divertor with the effect of heating power and pumping on the access to detachment in the Super-X configuration

E Havlíčková¹, J Harrison¹, B Lipschultz², G Fishpool¹, A Kirk¹, A Thornton¹, M Wischmeier³, S Elmore¹, S Allan¹

¹ Culham Centre for Fusion Energy, Culham Science Centre, Abingdon, OX14 3DB, United Kingdom

² Department of Physics, University of York, Heslington, York, YO10 5DD, United Kingdom

³ Max-Planck Institut für Plasmaphysik, Boltzmannstraße 2, D-85748 Garching, Germany

E-mail: eva.havlickova@ccfe.ac.uk

Abstract. SOLPS simulations of MAST-U have been carried out to identify in more detail the physics and operational properties of novel divertor configurations such as Super-X divertor (SXD), in particular the physics of detachment. A well diagnosed L-mode discharge from MAST has been utilised to determine L-mode transport coefficients representative for MAST-U L-mode plasmas. Simulations show that under the same core plasma conditions, the MAST-U SXD is strongly detached whilst the conventional divertor (CD) is not (1 eV vs 20 eV at the divertor plate). The detachment and higher power losses (1.6x) in the SXD vs the attached CD lead to a factor of 25 reduction in the target power load and are attributed to changes in radial location of the target. An attached regime can be established for the SXD in L-mode for higher pumping speed and/or heating power. In contrast, the simulation predicts that the MAST-U CD requires 3x higher density or 4x reduced power than the SXD to detach. Comparing two versions of the SXD, each with a different amount of poloidal expansion in the region near the divertor plate, we find that the effect of additional poloidal flux expansion of the SXD on an already detached plasma is small for a change in flux expansion in volume by a factor of 2-3 (target temperature 0.7 eV vs 1.1 eV). The poloidal flux expansion re-arranges the radiation pattern with only a small increase in divertor power losses (1.06x) compared to changing from the CD to SXD topology. By artificially increasing the leakage from the divertor chamber, we confirmed that the tight closure of the divertor region leads to strong increases in neutral density with concomitant power losses.

1. Introduction

The MAST-U experiment [1, 2] with its flexible divertor geometry will provide an opportunity to contribute to power exhaust physics in issues such as detachment or power handling which constitutes one of the most important problems for operation of DEMO-sized devices. The new divertor design in MAST-U enables the so-called Super-X divertor (SXD) [3] where the target power load is reduced, and detachment achieved, compared to a conventional divertor (CD). This is due to the combined effect of increased connection length, larger flux expansion and larger target radius [4] as well as larger volumetric power losses [5, 3]. The device will be also equipped with a new central column allowing for increased plasma current, pulse duration and toroidal field compared to MAST.

A modelling activity has been undertaken using SOLPS5.0 [6] to predict divertor conditions in MAST-U where two key divertor features are – (i) flexible magnetic topology in the divertor and (ii) improved divertor closure by baffling. Three magnetic configurations of MAST-U are considered – (i) a conventional divertor with small target radius and small flux expansion, (ii) a Super-X divertor with large target radius and large poloidal flux expansion (SXD1), (iii) a Super-X divertor with large target radius, but small poloidal flux expansion (SXD2). To decouple the effect of magnetic topology and neutral plugging in the divertor, an SXD divertor with the baffle removed is also analyzed (SXD3). The effect of the SXD on plasma parameters in both attached and detached conditions has been investigated by modelling in recent publications [7, 8], and high radiation cases with impurity seeding have been analyzed in [9, 10]. In this paper, predictions for MAST-U are made for the first time using simulation parameters derived directly from a benchmarking of the code against MAST experiment. For this purpose, a typical L-mode discharge has been utilised to obtain representative radial transport coefficients. Similar technique is used in [11, 12] in different collisionality regimes including detached cases. The physics of SOLPS5.0 and the equations used in the code are described in [6].

The magnetic topology of the divertor affects its operational regime and the access to detachment. Although attached plasmas are ultimately undesirable, the transition from attached conditions to detachment allows us to study the critical detachment process. Current MAST discharges are low in divertor power and temperature and it is expected that such conditions would lead to a detached plasma in MAST-U with the SXD. MAST-U will be, however, equipped with a system of cryopumps and a new NBI heating system. Pumping speed and input power scans are therefore performed to estimate the operating window where we would expect attached divertor conditions. Note that results presented in the paper are obtained for a representative L-mode case at constant density and radial transport, and therefore do not cover the whole operational space of MAST-U, especially H-mode plasmas. In addition, this study is representative of steady-state conditions and omits that the attachment window can be increased earlier in the discharge due to passive pumping.

2. L-mode experiment as described by SOL transport modelling

2.1. MAST experiment and simulation parameters

An NBI heated connected double-null MAST discharge 30356 has been selected as a test case for a comparison with SOLPS and for an extrapolation to MAST-U in section 3. Available diagnostics for this shot include Thomson scattering (TS), divertor Langmuir probes (LP) and infrared thermography (IR). Experimental data are taken in a quiescent period at 240 ms with the plasma current of 750 kA.

A simulation grid is shown in Fig. 1. The input power to the grid (the power crossing the core boundary) is assumed to be $P_{\text{inp}} = 1.7$ MW, which is derived as $P_{\text{inp}} \approx P_{\text{heat}} - P_{\text{rad}} - dW/dt$ where P_{heat} is the heating power, P_{rad} is the radiated power measured by bolometry and dW/dt is the rate of change of the stored magnetic energy from EFIT. P_{inp} is also estimated from IR measurements to reduce a possible error. For this discharge, the power arriving to the targets measured by IR is approximately 1.1 MW taking into account the wetted fraction of the divertor of 0.78. This also leads to $P_{\text{inp}} \approx 1.7$ MW if 35% power loss (as predicted by SOLPS) is assumed in the scrape-off layer (SOL). Therefore, the estimate from the expression above is consistent with the IR data for this discharge.

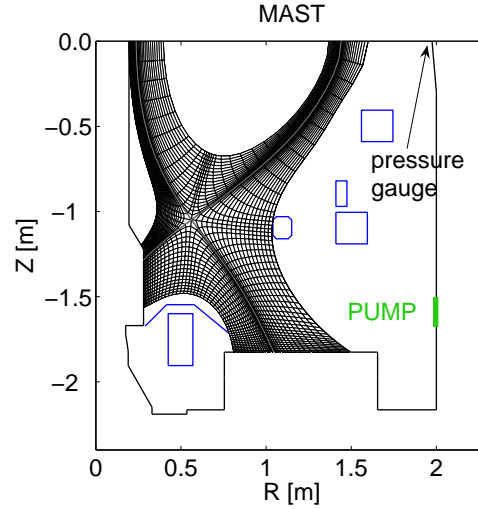


Figure 1. Simulation grid for the MAST discharge 30356. The position of the pump in the simulation and the position of the pressure gauge in the experiment are indicated.

Fuelling is simulated as a source from the core and its strength is adjusted to match the density at the core boundary $n_{\text{core}} = 1.3 \times 10^{19} \text{ m}^{-3}$ prescribed by the experimental profile from TS. The separatrix density in the simulation is approximately $0.7 \times 10^{19} \text{ m}^{-3}$. The pump in MAST is located in the lower part of the chamber (indicated in Fig. 1) and the pumping speed of $10.7 \text{ m}^3/\text{s}$ is assumed [13].

Radial transport coefficients in this MAST case are chosen to fit the experimental profiles of n_e and T_e from TS and are assumed to be poloidally uniform (see [14] for other discharges). The radial particle diffusivity is $4 \text{ m}^2\text{s}^{-1}$ everywhere and the radial

heat conductivity for both electron and ions is $10 \text{ m}^2\text{s}^{-1}$ inside the separatrix and $4 \text{ m}^2\text{s}^{-1}$ outside the separatrix.

Additional assumptions used in the simulation include: the carbon chemical sputtering coefficient of 3% (the simulation includes both chemical and physical sputtering from the walls and targets), the heat flux limiters of 0.3 and 1.0 for electron and ions, the viscous ion flux limiter of 0.5 (this corresponds to a moderate limiting typically used in SOL simulations, the limiters are defined in [6]). The sensitivity of results to the choice of the pumping speed, the chemical sputtering coefficient and the flux limiters is discussed in the appendix which also describes additional simulation results such as the distribution of power losses in the grid, or atomic and molecular densities at the midplane and in the divertor. Finally, a simulation without drifts is considered, while the effect of drifts for MAST is extensively studied elsewhere [15].

2.2. Comparison of simulation results and experimental data

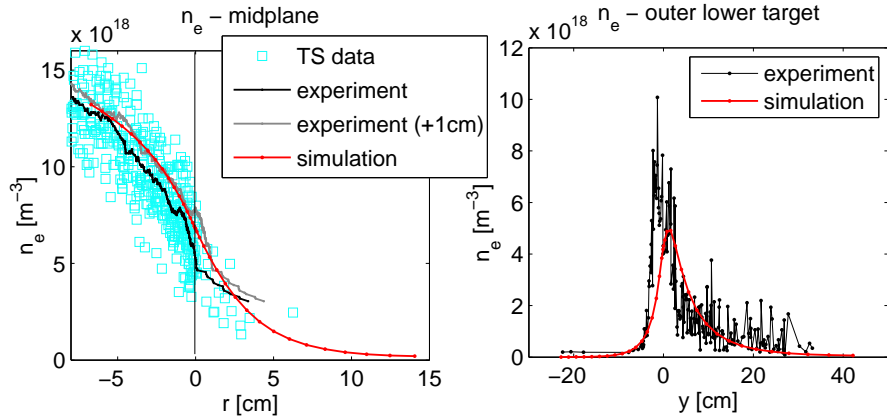


Figure 2. Radial profiles of the electron density from the experiment and simulation at the midplane (left) and at the target (right).

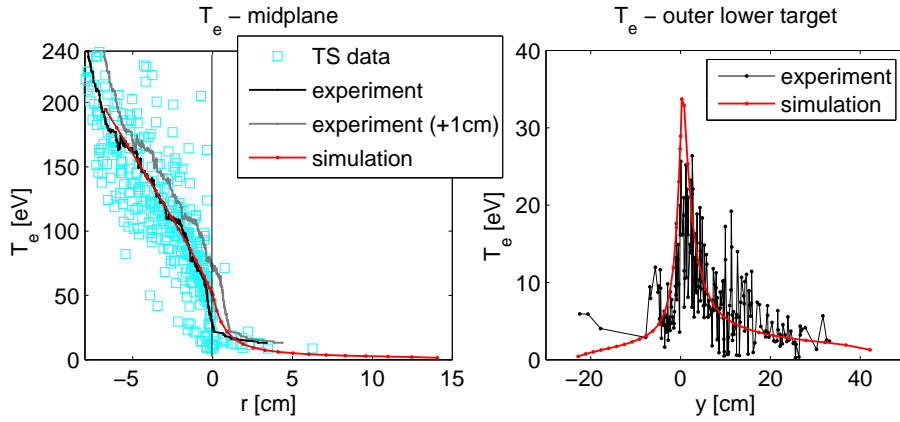


Figure 3. Radial profiles of the electron temperature from the experiment and simulation at the midplane (left) and at the target (right).

Experimental profiles of the density and temperature at the outer midplane are obtained by averaging TS profiles to remove scatter in the raw data. The profiles are shown in Figs. 2 and 3 on the left (black) with the raw TS data (cyan) and are overlaid by simulation results (red). On the right, target profiles from LP are shown. The experimental profiles at the midplane are also shown shifted by 1 cm with respect to the original position to take into account an uncertainty in the separatrix location. Eventually, this uncertainty can be used to match the target parameters better, and typically, a 1 cm error is allowed based on the accuracy of the equilibrium reconstruction. Figs. 2 and 3 show reasonable agreement between SOLPS and the experiment within errors in the measured data, the separatrix location and uncertainties in simulation parameters.

The simulated energy flux at the target compares very well with the IR measurement (Fig. 4 left) for the given P_{imp} and χ_{\perp} , and the IR data is in good agreement with the LP data (Fig. 4 right). Note that both the LP and IR measurements are symmetric between the lower and upper divertors in this double-null discharge, therefore only the data from the lower divertor are used for comparison. The simulated λ_Q calculated as $\lambda_Q = \int Q_t dy / Q_t^{\text{max}}$ and mapped to the midplane is 1.7 cm and can be compared with other MAST discharges in [16].

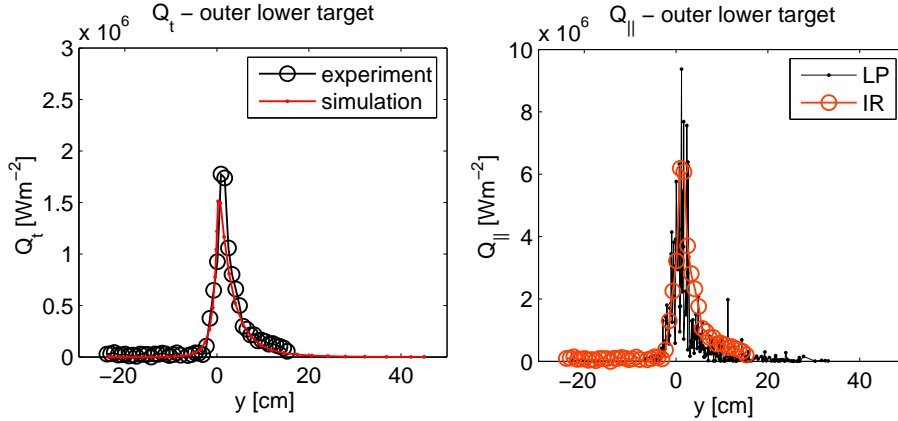


Figure 4. Comparison of the simulated energy flux at the outer target deposited by electrons and ions and the one measured by IR (left), comparison of the energy flux at the target measured by IR and LP (right) with the LP signal calculated as $Q_{||} = 7T_e n_e c_s$. Q_t is the energy flux normal to the target, while $Q_{||}$ is the parallel energy flux.

Also the simulated $\text{D}\alpha$ emissivity fits well the experimental measurement at the midplane (Fig. 5). A shift between the peak values of 1 cm supports the assumption that a shift of the equilibrium with respect to the experimental profiles of 1 cm can be allowed.

Finally, the molecular density in the simulation is compared with a measurement from the pressure gauge located in the main chamber at the midplane (Fig. 1). Since the density outside the plasma grid is not directly available in the simulation, we compare the experimental value of $1.3 \times 10^{18} \text{ m}^{-3}$ with the simulated value at the boundary of

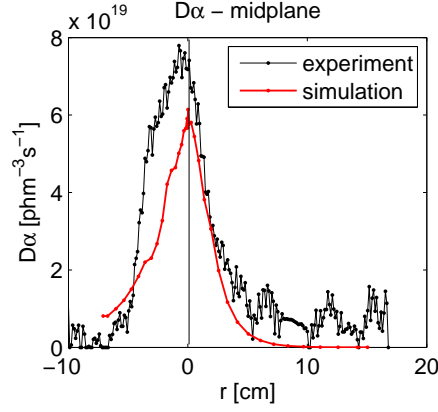


Figure 5. Comparison of the measured and simulated $D\alpha$ emissivity at the outer midplane.

the grid of $1.6 \times 10^{18} \text{ m}^{-3}$ (see Fig. 18). Unfortunately, the data from a pressure gauge located in the divertor chamber are unavailable for comparison.

Good agreement between the experiment and modelling has been found for available diagnostics data including densities and temperatures in the scrape-off layer, energy fluxes to the target, $D\alpha$ radiation or molecular density at the midplane. This gives a basis to predict conditions in the MAST-U divertor in the next section.

3. Predictions for MAST Upgrade

3.1. Divertor geometry in MAST Upgrade

In comparison to MAST (Fig. 1), MAST-U will operate with a closed divertor (Fig. 6) and a system of cryopumps in both lower and upper divertor chambers. Apart from

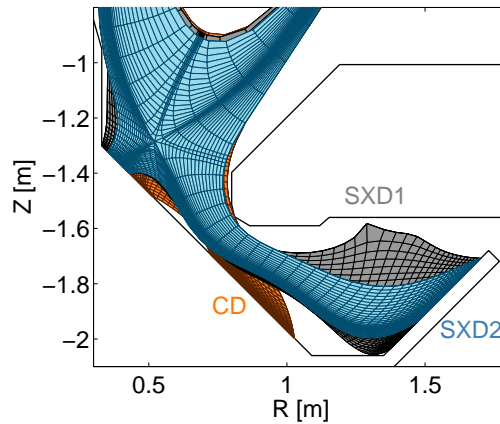


Figure 6. Magnetic geometry in the MAST-U divertor considered in the simulation: CD (orange), SXD1 (black), SXD2 (blue).

the closed design and increased pumping efficiency, conditions in the outer divertor can be influenced by the magnetic topology which can be optimized in order to reduce

plasma temperatures and heat fluxes at the target plate. Three magnetic topologies with different connection length, flux expansion and strike point radius are considered in the simulation (Figs. 6 and 7).

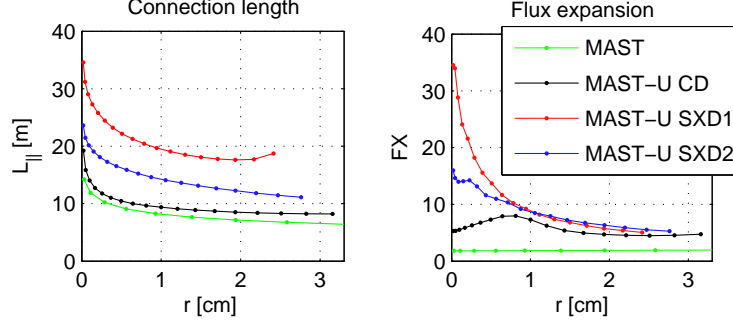


Figure 7. The midplane to target connection length (left) and the total flux expansion (right) in the outer SOL in MAST from Fig. 1 and MAST-U from Fig. 6.

	$\langle FX \rangle$	$\langle FX \rangle_{\text{pol}}$	$\langle FX \rangle_{\text{tor}}$	$\langle FX \rangle_{\text{tilt}}$	$\langle dy/dr \rangle$
MAST	1.8	2.3	0.7	1.1	2.9
MAST-U CD	6.6	3.3	0.6	3.1	12.5
MAST-U SXD1	20.2	5.9	1.2	2.8	20.5
MAST-U SXD2	12.4	2.4	1.2	4.3	12.2

Table 1. Flux expansion factors in the outer SOL averaged over 1 cm of the radial distance at the midplane. $\langle FX \rangle$ is the total flux expansion, $\langle FX \rangle_{\text{pol}}$ and $\langle FX \rangle_{\text{tor}}$ is the poloidal and toroidal magnetic flux expansion, $\langle FX \rangle_{\text{tilt}}$ is the flux expansion caused by the target tilting, $\langle dy/dr \rangle$ is the expansion related to the projection from the radial midplane coordinate r to the target coordinate y . The total flux expansion can be approximately calculated as $\langle FX \rangle \approx \langle FX \rangle_{\text{pol}} \times \langle FX \rangle_{\text{tor}} \times \langle FX \rangle_{\text{tilt}}$ and the exact definitions are given in [7].

In Fig. 7 and Tab. 1, the flux expansion in the divertor of MAST-U is also compared with the equilibrium obtained for the MAST shot 30356 described in the previous section. The separation into the poloidal magnetic flux expansion, the toroidal magnetic flux expansion and the flux expansion caused by the target tilting (Tab. 1) shows that the total flux expansion in the CD is increased compared to MAST mainly due to the target tilting. In the SXD1, the flux expansion increases further due to larger radius of the target plate (larger toroidal flux expansion) and due to reduced poloidal field in the divertor (larger poloidal flux expansion). The SXD2 is an intermediate case between the CD and SXD1 with larger toroidal flux expansion, but smaller poloidal flux expansion.

In addition to the magnetic topologies CD, SXD1 and SXD2, we also consider a simulation of the SXD where the baffle is removed, assuming the magnetic topology of the SXD1. This case will be labelled as SXD3.

3.2. Low power case

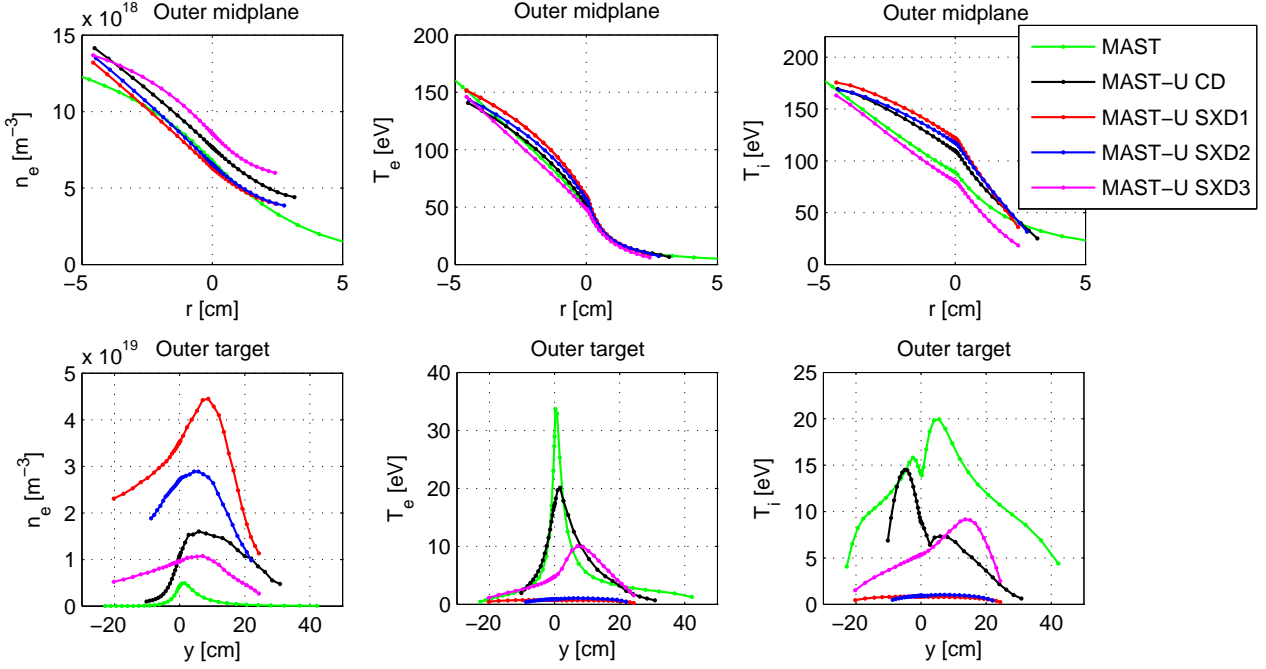


Figure 8. Radial profiles of the electron density (left), the electron temperature (middle) and the ion temperature (right) at the outer midplane (top) and at the outer target (bottom). The radial midplane coordinate r and the target coordinate y measure the distance from the separatrix which is represented by 0.

Simulation parameters used for MAST-U are the same as in the simulation of the MAST discharge 30356 ($P_{\text{inp}} = 1.7$ MW, $n_{\text{core}} = 1.3 \times 10^{19} \text{ m}^{-3}$), only the magnetic topology is changed and the pumping efficiency is increased from $10.7 \text{ m}^3\text{s}^{-1}$ used in MAST to $42 \text{ m}^3\text{s}^{-1}$ in MAST-U to take into account larger pumping speed available in MAST-U. Fig. 8 shows simulated radial profiles of the density and temperature at the outer midplane and along the outer target. While similar upstream densities and temperatures are obtained regardless of the divertor geometry, the divertor parameters change significantly. The electron temperature at the target drops to approximately 1 eV in MAST-U with the SXD, and similar divertor temperatures are achieved in the SXD1 (0.8 eV) and SXD2 (1.1 eV). This suggests that an additional poloidal flux expansion inside the SXD in MAST-U does not have a strong effect on the access to detachment (this has been already shown in [9] for an impurity seeded transition to detachment).

MAST-U with the CD is still attached with the target temperature of 20 eV. The difference between the CD and the shot 30356 (labelled as MAST) is perhaps not as large as one would expect from open vs closed divertor. This comes from a combination of larger divertor closure with respect to neutrals in the CD case (increasing the neutral pressure), but also stronger pumping in MAST-U (reducing the neutral pressure). The CD therefore achieves rather similar divertor parameters as MAST, but what changes

dramatically is the ratio between the divertor and upstream atomic and molecular pressures.

Fig. 8 also indicates that the amount of neutrals in the divertor is an important factor for the access to detachment, as the SXD without the baffle (labelled as SXD3), where neutrals are free to escape the divertor, is attached. The baffle causes a drop of the electron temperature at the target from 10 eV to 1 eV and an increase of the target density from $1.1 \times 10^{19} \text{ m}^{-3}$ to $4.4 \times 10^{19} \text{ m}^{-3}$, proving a strong role of neutrals in reducing the divertor temperature and the detachment threshold. This could also explain the difficulties to make the outer divertor detach in current MAST discharges.

The SXD2 with low poloidal flux expansion differs only slightly from the flux-expanded one in terms of the divertor temperatures and the divertor closure with respect to neutral species, and the main effect of the additional poloidal flux expansion is in a reduction of the energy flux to the target (discussed later). The effect of the additional flux expansion, compared to the effect of larger target radius, depends on the collisionality regime; In detached cases with high power losses, the effect of the flux expansion is weaker than the effect of radiation and plasma-neutral interactions which set the conditions in the divertor. The importance of plasma-neutral interactions in MAST-U is due to its closed divertor design.

The divertor closure is shown in Fig. 9 and is measured as the ratio of the ionization source outside the divertor (including the core and upper SOL part of the grid) and the total ionization source in the grid. The effect of the baffle in MAST-U is clearly visible (see MAST and SXD3). The SXD1 and SXD2 configurations achieve similar level of the closure, while the closure in the CD is slightly weaker due to shorter distance between the target and the X-point and larger ionization mean free path (larger temperature and smaller density in the CD). Note also that in the CD, neutral densities in the divertor are smaller than in the SXD, but comparable at the X-point and in the core.

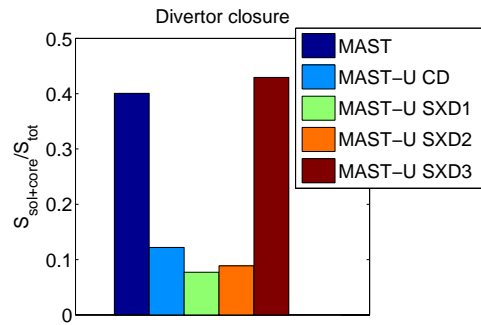


Figure 9. Divertor closure with respect to neutrals calculated as the ionization source in the simulation grid outside the divertor region with respect to the ionization source in the whole grid.

A reduction of the energy flux to the outer target related to the modification of the divertor geometry is shown in Fig. 10 and is partly caused by the magnetic topology (see the flux expansion in Tab. 1), but also by power losses due to radiation, ionization and

charge exchange. The peak target energy flux drops from 1.5 MWm^{-2} in the simulation of the shot 30356 to 0.5 MWm^{-2} in MAST-U with the CD (a factor of 3, equal to the effect of the flux expansion), and is further reduced to 17 kWm^{-2} in the SXD1 or similarly to 21 kWm^{-2} in the SXD2 (a factor of 25, due to the flux expansion and power losses). This large drop is caused by the transition to detachment and shows the importance of strong volumetric power losses in comparison to the effect of magnetic flux expansion.

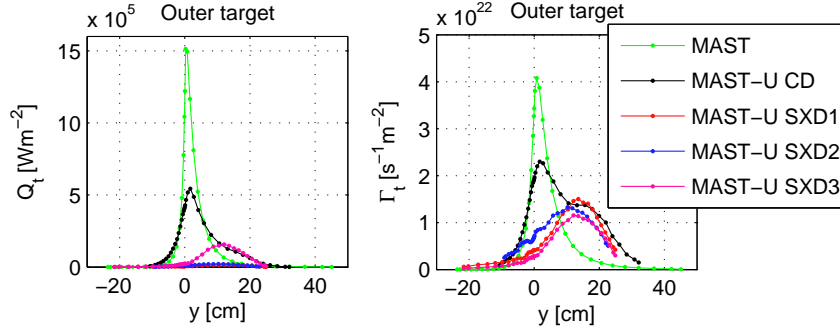


Figure 10. Radial profiles of the energy (left) and particle (right) fluxes at the outer target. Fluxes normal to the target surface are shown.

Power balance in MAST and MAST-U combining attached (MAST, CD, SXD3) and detached cases (SXD1, SXD2) is presented in Fig. 11 with the power to solid surfaces shown in blue and the power loss shown in yellow (the power radiated by carbon ions), orange (the power radiated by neutral species) and red (the power loss caused by ionization and charge exchange). The graph shows a reduction of the power deposited at the outer target in MAST-U compared to MAST (dark blue), especially with the SXD, accompanied by an increase in the radiated power in MAST-U thanks to the increased flux expansion and the baffle (the larger the neutral pressure in the divertor, the more radiation and cooling). The total power loss increases by nearly a factor of 2 in the SXD compared to the CD and is similar in the two SXD configurations. Strong neutral leakage from the SXD represented by the SXD3 case reduces the power loss by a factor of 1.5, to a similar level as the CD with the baffle. Thus it appears that the neutrals can have an effect on the divertor solution similar in strength to significant changes in R in going from the CD to SXD.

In Fig. 11, the MAST-U configurations receive less power to the outer targets, especially the SXD cases, but more power leaves the grid radially as P_{wall} and can be potentially deposited at the main chamber wall. Note that this is likely due to a narrower grid in MAST-U. Because the grid does not extend to the actual wall, we cannot directly determine the power reaching the wall and thus an accurate measure of P_{wall} . Instead, utilising a simple extrapolation technique, we made a maximum estimate of the power radiated outside the grid. We found that, if the radiation level does not decay between the grid boundary and the main chamber wall, the power radiated beyond the grid boundary can be substantial, potentially accounting for all the power leaving the grid.

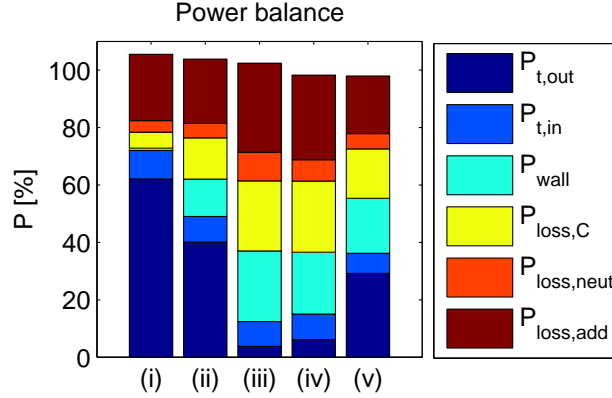


Figure 11. Power balance in the simulation of MAST (i), MAST-U with the CD (ii), MAST-U with the SXD1 (iii), MAST-U with the SXD2 (iv) and MAST-U with the SXD3 (v) with the input power $P_{inp} = 1.7$ MW. $P_{t,out}$ and $P_{t,in}$ is the power to the outer and inner target, P_{wall} is the power leaving the grid radially, $P_{loss,C}$ is the power radiated by carbon ions (line radiation), $P_{loss,neut}$ is the power radiated by neutral species (line radiation, three-body recombination, molecular dissociation), $P_{loss,add}$ is an additional power loss caused by plasma-neutral interaction (ionization, charge exchange). Note that P_{wall} includes both the energy flux deposited by the plasma at solid surfaces and the power radiated outside the plasma grid due to limited grid size. Therefore the increase in P_{wall} from MAST to MAST-U can be partly due to a narrower grid in the MAST-U cases. Also note that only the main power balance components are shown and for example viscous heating is not included in the graph, that is why the components do not sum up to 100% exactly.

However, the uncertainties in this extrapolation are large. A simulation with a grid extending up to the wall would be required for a confident quantitative estimate.

The distribution of the radiated power in the divertor can be compared in Fig. 12 for MAST-U and Fig. 17 for MAST. Total radiation is shown (left) as well as its components that are separated in the simulation as line radiation from carbon ions (middle) and radiation from neutral species (right). The radiation pattern shows an attached plasma in the CD and SXD3 radiating mainly around the strike point, while the radiation in the SXD1 and SXD2 takes place inside the divertor leg. The SXD provides larger radiation volume than the CD (the radiation zone is extended in the SXD in the direction of the magnetic field), which is consistent with the increased radiated power in Fig. 11. Finally, one observes a radial broadening of the radiation zone with the poloidal flux expansion in the SXD1 compared to the SXD2. However, this broadening does not significantly change the total radiated power for the detached SXD cases (Figs. 11 and 12). The total power loss is increased only by a factor of 1.06 in the SXD2 with respect to the SXD1. In contrast, the change from an attached CD to a detached SXD corresponds to an increase in power losses by a factor of 1.6.

We have also analyzed the radiated power in the flux-expanded region in more detail. Fig. 13 on the left shows the radiated power in the SXD1 and SXD2 integrated from the X-point towards the target as a function of the poloidal coordinate. Also shown are the radiation profiles across the divertor leg at $R = 0.9$ m (middle) and $R = 1.3$ m

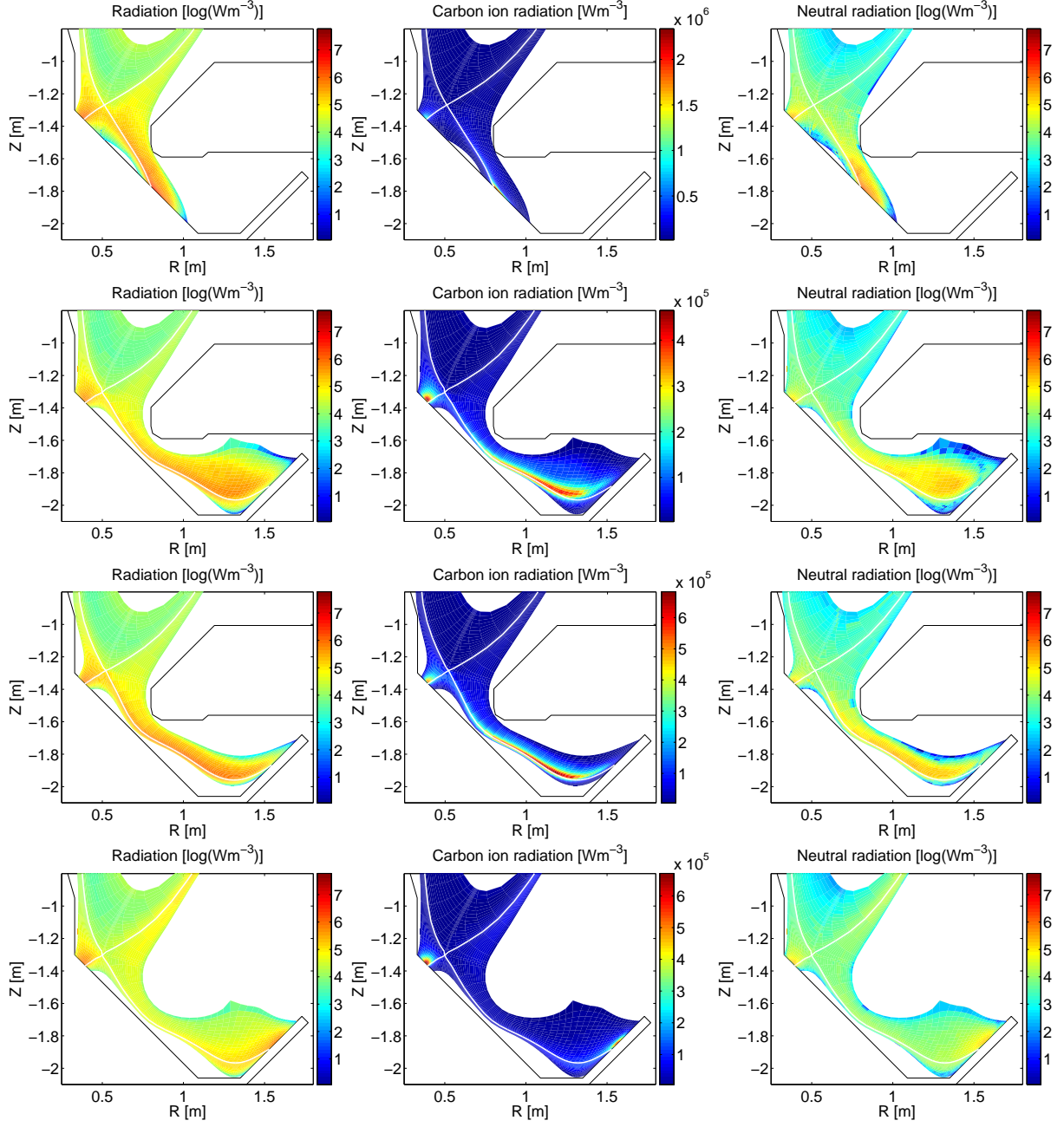


Figure 12. The distribution of the total radiation (left) and its components – the carbon ion line radiation (middle) and the radiation from neutral species (right) – in the MAST-U divertors – (i) CD, (ii) SxD1, (iii) SxD2, (iv) SxD3. Compare with Fig. 17 for the standard MAST divertor.

(right). The data confirm a broadening of the radiation profile inside the flux-expanded region (right). The amplitude of the radiated power density is however smaller in the SxD1 towards the X-point at the end of the poloidal flux-expanded region (middle). While the integral of the radiation profile just inside the flux-expanded zone in Fig. 13 on the right increases by a non-negligible factor of 1.6 in the SxD1 compared to the SxD2, the power loss integrated across the whole flux-expanded region increases only

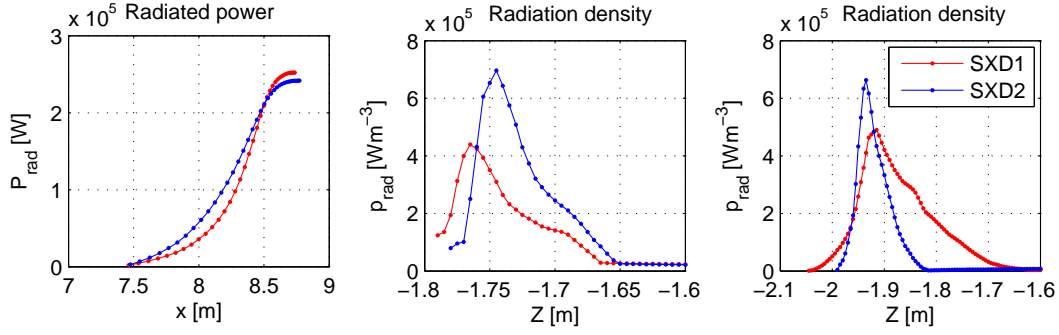


Figure 13. On the left, radiated power in the SXD1 and SXD2 as a function of the poloidal coordinate integrated between the X-point and the poloidal distance x . The coordinate x ranges from the X-point to the target. In the middle, a radiation profile taken vertically across the divertor at $R = 0.9$ m. On the right, a radiation profile taken vertically across the divertor at $R = 1.3$ m.

by a factor of 1.13. The radiative losses are then clearly redistributed by poloidal flux expansion in the divertor, however, the overall effect on the power loss in this case is small.

Finally, while not shown explicitly here, we find that carbon radiation is more effectively confined inside the divertor region in the SXD configurations (SXD1 and SXD2) than in the CD. We draw this conclusion because the total radiation on the grid from impurities in the SXD cases is almost a factor of 2 larger than for the CD divertor, while radiation in the core part of the grid is lower for the SXD than for the CD.

3.3. High power case

There are several ways to reduce temperatures in the divertor and access a detached regime, for example increasing the gas puff density, reducing the heating power or puffing additional impurities [17, 18]. In MAST-U, the transition to detachment can be also induced by modifications of the divertor magnetic topology.

Based on the study of MAST-U at power levels of MAST, the SXD topology would appear to always lead to detachment at low heating power. We now address what the effect of higher power levels would be on the divertor configurations from Fig. 6. We also assume slightly increased density $n_{\text{core}} = 1.7 \times 10^{19} \text{ m}^{-3}$ due to higher current of 1MA in the simulated MAST-U cases. Fig. 14 shows that the SXD1 is just around the detachment threshold with the peak electron temperature at the target $T_e \approx 4.5$ eV. This means that an attached regime can be obtained in the SXD at the given density if the heating power or the pumping speed is increased further (see power and pumping scans in the next section).

As a measure of a reduction of the detachment threshold in the SXD, we also examined how much the density has to be increased or the input power lowered in the CD from Fig. 14 to achieve target temperature of around 5 eV as in the SXD1 case. Based on SOLPS calculations, we found that the CD with 3.5 MW of the input

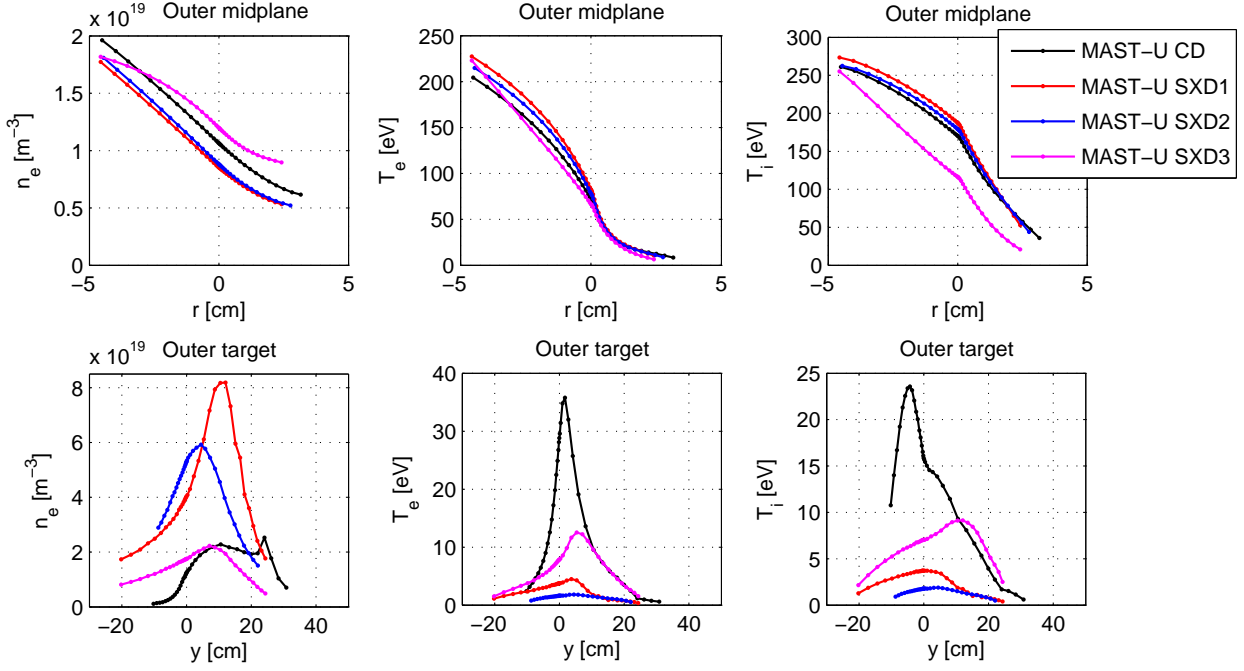


Figure 14. Radial profiles of the electron density (left), the electron temperature (middle) and the ion temperature (right) at the outer midplane (top) and at the outer target (bottom).

power would allow the access to detachment at approximately 3 times higher separatrix density n_{sep} than the SXD1 (corresponding to 3-4 higher n_{core}). Similar result was obtained in [8] for a MAST-U case with narrow SOL. Alternatively, at the given density of $n_{\text{core}} \approx 1.7 \times 10^{19} \text{ m}^{-3}$ and $n_{\text{sep}} \approx 1 \times 10^{19} \text{ m}^{-3}$, the transition to detachment would occur in the CD at approximately 4 times lower input power. These factors are slightly higher than those calculated from the modified two-point model [4] that accounts for the effect of varying target radius and which gives a factor of 2.2 increase of the separatrix density and a factor of 3.1 reduction of the input power (assuming the connection length $L_{\parallel} \approx 20$ m in the CD and $L_{\parallel} \approx 35$ m in the SXD1, and the target radius $R_t \approx 0.8$ m in the CD and $R_t \approx 1.53$ m in the SXD1). Note that the target temperature in the two-point model is modified only as the result of geometry, taking into account the target radius and the connection length, while in SOLPS, both geometric effects and cooling due to plasma-neutral interactions are involved. In [9], the effect of the SXD topology on the detachment threshold in a nitrogen seeded plasma has been studied, resulting in a factor of 7 lower nitrogen seeding rate required for the outer leg to detach in the SXD compared to the CD.

4. Dependence of detachment on input power and pumping in the MAST-U Super-X divertor

As part of the study of the detachment threshold in MAST-U, we examined the effect of varying the amount of input power and cryopumping on the SXD case (SXD1) only.

Fig. 15 presents the results of an input power scan where the divertor temperature (Fig. 15 right) is varied due to increases in the upstream temperature (Fig. 15 left). The density is not influenced by increasing power. Fig. 15 shows that attached conditions can be achieved in the SXD at higher power levels, for this particular L-mode case for the input power above 3.5 MW. The maximum heating power available in MAST-U will be 12 MW and it is expected that 4-8 MW will cross the separatrix as the input power P_{inp} due to charge-exchange and radiation losses in the core plasma.

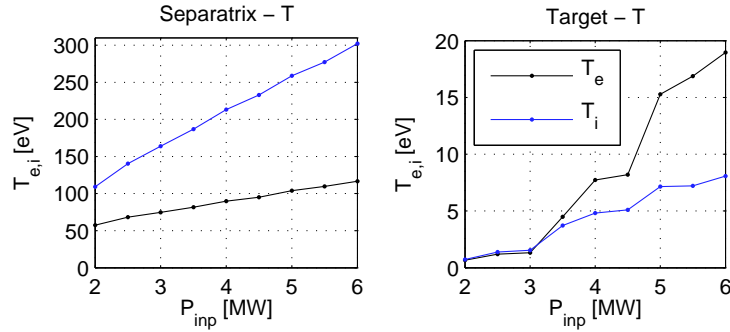


Figure 15. The upstream (left) and the peak target (right) electron and ion temperatures as functions of the input power in the simulation of the SXD1 with the pumping speed of $42 \text{ m}^3\text{s}^{-1}$.

An increase of the pumping speed on cryopumps (Fig. 16) modifies both target density (Fig. 16 left) and temperature (Fig. 16 right), while the upstream values are not affected. The MAST-U design value for the cryopump is $50\text{-}60 \text{ m}^3\text{s}^{-1}$ which increases the divertor temperature over the level of pumping used in this study (Fig. 16).

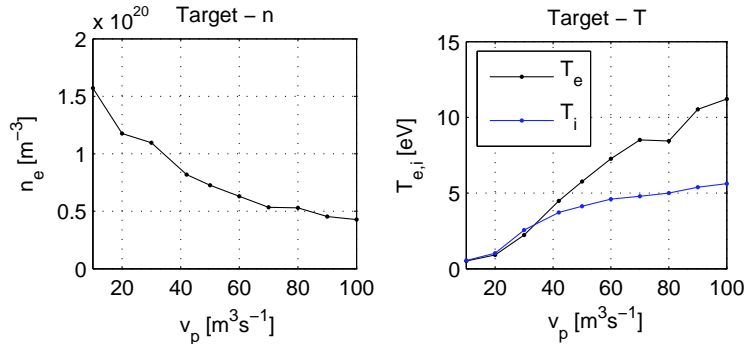


Figure 16. The peak target electron density (left) and the peak target electron and ion temperatures (right) as functions of the pumping speed in the simulation of the SXD1 with the input power of 3.5 MW.

Note that the effect of the density and the SOL width is not investigated in this study. We also speculate, that the operational space in attached plasmas would be broader in H-mode due to typically narrower SOL, see [16, 19], which would lead to larger upstream and peak target temperatures for the same input power. Re-attachment during ELMS is another possibility to study the transition from attached to detached conditions. Alternatively, the attachment window would be extended during time-dependent passive pumping in the discharge before reaching a steady-state phase studied.

5. Conclusions

A SOLPS simulation of the MAST L-mode discharge 30356 has been successfully benchmarked against experimentally measured data. A good agreement has been achieved between the code results and all available diagnostics including Thomson scattering profiles, Langmuir probes divertor profiles, $D\alpha$ measurement, infrared camera data and molecular density measurement. This comparison is used to obtain a set of radial transport coefficients representative of MAST L-mode plasmas, which gives a good basis to predict conditions in the MAST-U divertor, again for L-mode conditions. Both the conventional and Super-X topologies are investigated for MAST-U.

Modelling results show that the MAST-U divertor exhibits dramatically better closure with respect to neutral species compared to the open MAST divertor, thanks to baffling, and achieves larger power losses and a reduction of the target power load. The divertor operational regime can be further influenced by a modification of the divertor magnetic geometry; The power load to the target is significantly reduced in the SXD of MAST-U (a factor of 25) compared to the CD as the result of plasma detachment. The radiation zone expands in the SXD compared to the CD and the total radiated power nearly doubles. In the studied case of a low power detached SXD L-mode plasma, addition of poloidal flux expansion leads to an increase in power losses small compared to changes in topology studied (e.g. CD to SXD). This could be because either the flux expansion just re-arranges the existing radiation or that in detached regimes the radiation integrated along each flux tube saturates at a level approaching the parallel heat flux further upstream. Since the additional poloidal flux expansion does not strongly modify the target temperature for the SXD case studied, we speculate that it might also not influence the access to detachment. However, the effect of poloidal flux expansion on the detachment threshold requires further studies where the same attached condition is achieved for SXD and CD topologies.

Simulations based on the comparison of SOLPS with an L-mode MAST discharge predict detached divertor operation in the SXD of MAST-U, while the CD configuration with a short outer leg and smaller target major radius achieves rather similar divertor conditions as MAST. The addition of neutral leakage from the divertor has a strong effect on the access to detachment, such that the SXD divertor without the baffle would be attached. In L-mode, an attached plasma can be obtained in the SXD with the baffle as well, utilising levels of heating power and pumping efficiencies planned for

MAST-U. Note that these predictions are based on a single comparison between the code and experiment for a typical L-mode case and are carried out assuming steady-state conditions. We expect that in H-mode with narrower SOL, higher peak target temperatures for the same power crossing the separatrix, as well as transients, would make SXD attached divertor operation available at lower input power and/or lower cryopumping speed. Finally, the simulation of MAST-U in L-mode shows that the SXD configuration lowers the detachment threshold by approximately a factor of 3 in the density and a factor of 4 in the input power compared to the CD configuration.

Acknowledgments

This project has received funding from the European Union’s Horizon 2020 research and innovation programme under grant agreement number 633053, from the RCUK Energy Programme [grant number EP/I501045] and from the Wolfson Research Fellowship. The views and opinions expressed herein do not necessarily reflect those of the European Commission. The author gratefully acknowledges the support of X. Bonnin and D. Coster.

Appendix

Additional simulation results for the discharge 30356

Additional simulation results, for which no comparison with experiment is available, are presented in this section.

The simulation of the 30356 discharge leads to the total power loss in the grid of 35% (10% in the core part of the grid, 9% in the SOL above the X-points, 2% in the inner divertors, 13% in the outer divertors). Outer targets receive approximately 62% of the power and 10% is deposited at the inner targets, excluding the power from the ion viscous flux which is treated separately in the simulation as a viscous heating term and reaches 8%. The power leaving the grid radially is smaller than 1%, negligible compared to the power to the targets. Not all the power loss is due to radiation. The total radiated power in the grid is approximately 10% (2% in the core, 1.7% in the SOL above the X-points, 1.2% in the inner divertors, 5% in the outer divertors). 6% of the input power is radiated by carbon ions and 4% is radiated by neutral species (D, C, D₂). Approximately 24% of the power is lost due to other processes than radiation, such as ionization and charge exchange. The radiation pattern is shown in Fig. 17 where the radiated power is separated into radiation from carbon ions and neutral species. Plasma is attached and the radiation is strongest around the strike points at the targets. The distribution in the divertor can be compared with MAST-U cases in section 3.2.

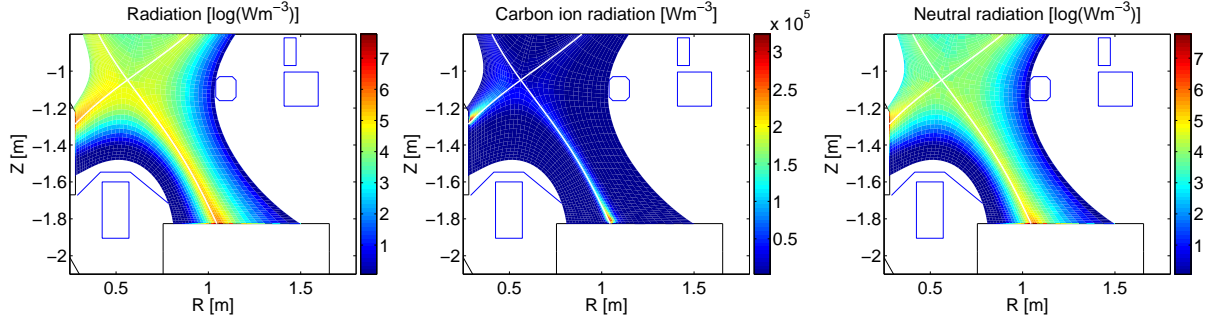


Figure 17. The distribution of the total radiation (left) and its components – the carbon ion line radiation (middle) and the radiation from neutral species (right) – in the MAST divertor.

Fig. 18 shows the atomic and molecular density at the midplane and target. Atomic and molecular densities at the separatrix are of the order of 10^{16} m^{-3} and saturate at approximately $0.9 \times 10^{17} \text{ m}^{-3}$ (deuterium atoms) and $1.6 \times 10^{18} \text{ m}^{-3}$ (deuterium molecules) outside the separatrix. The neutral and molecular densities at the target are of the order of 10^{18} m^{-3} . It should be noted that the divertor closure of MAST with respect to neutral species is much weaker compared to MAST-U where the neutral compression between the divertor and the midplane is increased thanks to a baffle that reduces the leakage of molecules and atoms from the divertor chamber. As the result, the atomic and molecular densities in the core in MAST are larger than in MAST-U by

an order of magnitude, in spite of smaller densities in the divertor.

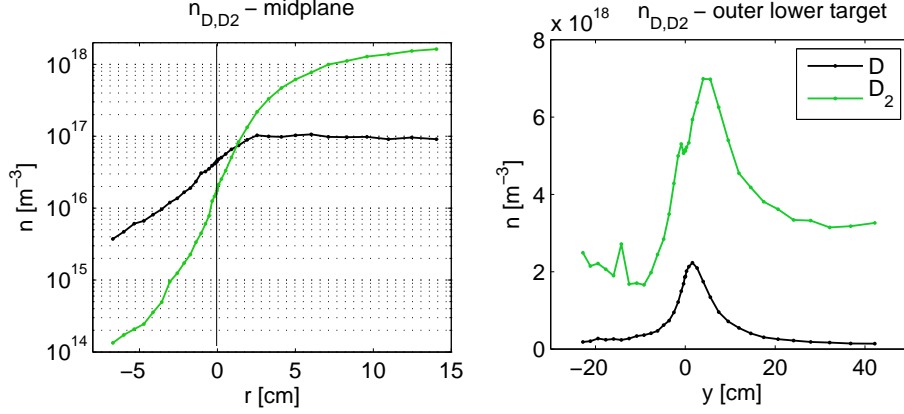


Figure 18. Radial profiles of the atomic and molecular density at the outer midplane (left) and outer target (right).

Sensitivity of results to simulation parameters for the discharge 30356

Some of the previous simulations of MAST-U [7] and MAST discharges resulted in large temperatures in the SOL compared to values typically observed in MAST experimentally. One of the reasons was that in MAST, the power that crosses the separatrix can often be much smaller than the heating power due to large dW/dt . Second, there is a certain freedom in the separatrix position, hence the separatrix density and temperature. Third, L-mode discharges such as 30356 require relatively large radial heat diffusivity χ_{\perp} in the simulation inside the separatrix to reproduce experimentally observed slope in the temperature profiles. Large heat diffusivity in the edge region of the core is also supported by TRANSP simulations [20]. Finally, uncertainties in simulations parameters or missing physics in the code could be responsible for deficiencies in precise quantitative description of the experiment.

This motivates us to examine the sensitivity of solution for the discharge 30356 to simulation parameters which are unknown from experiment. Among these are flux limiters in Figs. 19 and 20 for which no systematic study exists and their choice is to a certain extent intuitive. The electron heat flux limiter in Fig. 19 does not have a strong effect on the solution due to small parallel temperature gradients in the sheath-limited case. In addition, the electron heat flux limiter is not required in middle to high collisionalities [21]. The ion heat flux limiter has a large effect on both upstream and target ion temperature and its choice is important if a comparison with experiment for T_i is concerned. The effect of viscous flux limiter is shown in Fig. 20. Stronger limiting with $\beta = 0.1$ is not much different from the reference value of 0.5 and values below 0.1 are unlikely based on a comparison of fluid and kinetic models [21]. Weaker limiting with $\beta = 2.0$ increases the target temperature and reduces the target density by 20–30%. From a comparison between kinetic and fluid codes, the value 0.5 or lower

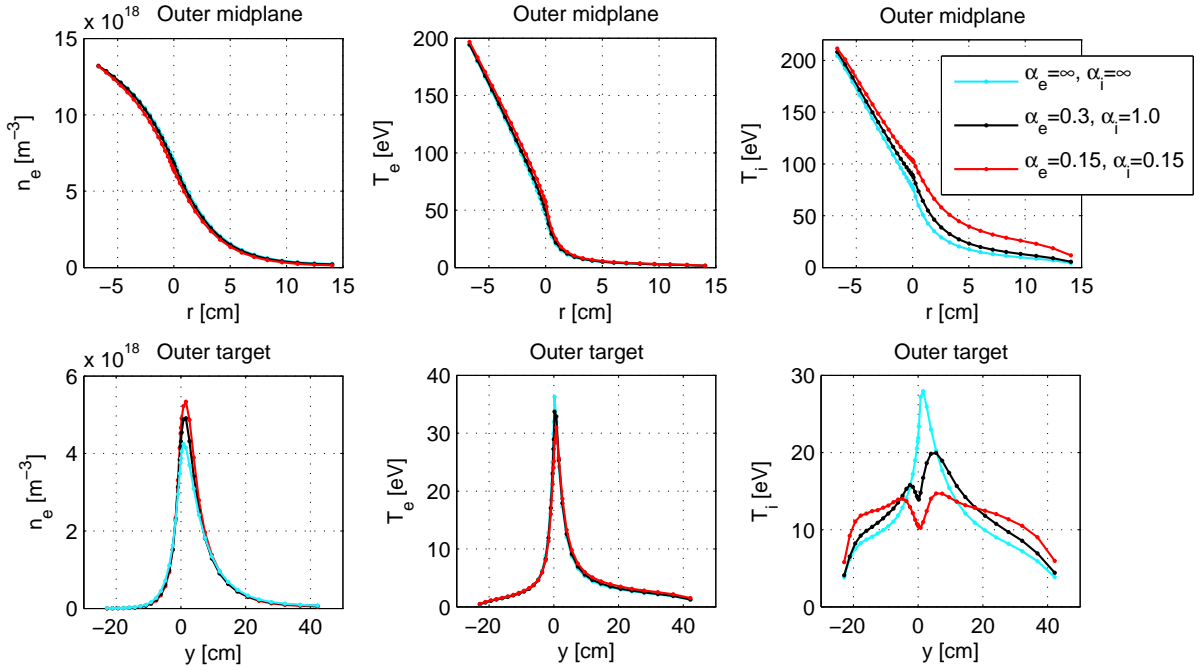


Figure 19. Radial profiles of the density and temperature at the outer midplane (top) and outer target (bottom) in the simulation with different heat flux limiters.

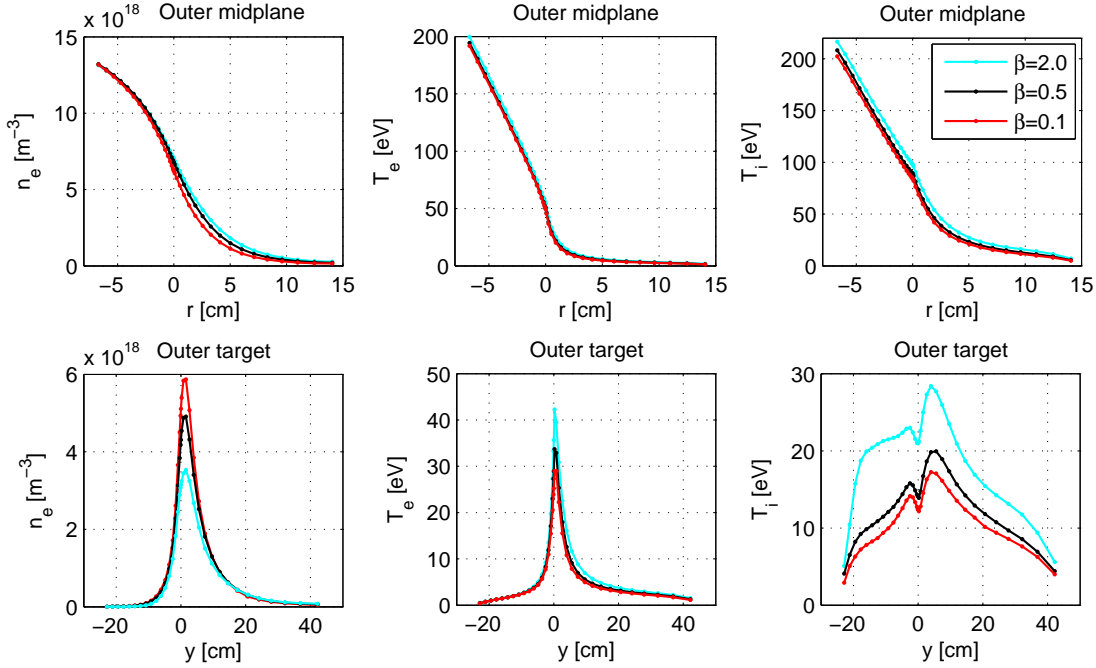


Figure 20. Radial profiles of the density and temperature at the outer midplane (top) and outer target (bottom) in the simulation with different viscous flux limiters.

is more appropriate for a case without recycling (sheath-limited), while larger values are appropriate only for high-recycling cases [21].

The effect of the sputtering yield coefficient and pumping speed on the divertor

temperature is tested in Figs. 21 and 22. It is shown that none of these parameters significantly influence the solution within a range of values that are realistic. The pumping speed in MAST is already low so that its further reduction does not reduce the divertor temperature. The increase of the sputtering yield from 1 to 5% reduces the target temperature only by approximately 20%.

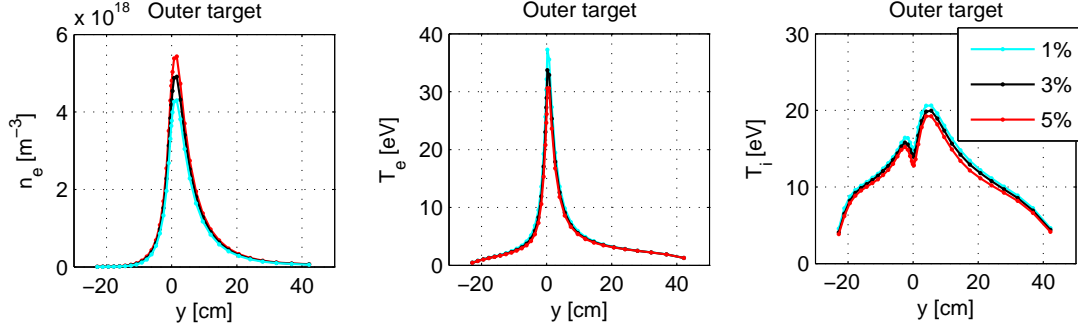


Figure 21. Radial profiles of the density and temperature at the outer target in the simulation with different chemical sputtering yield.

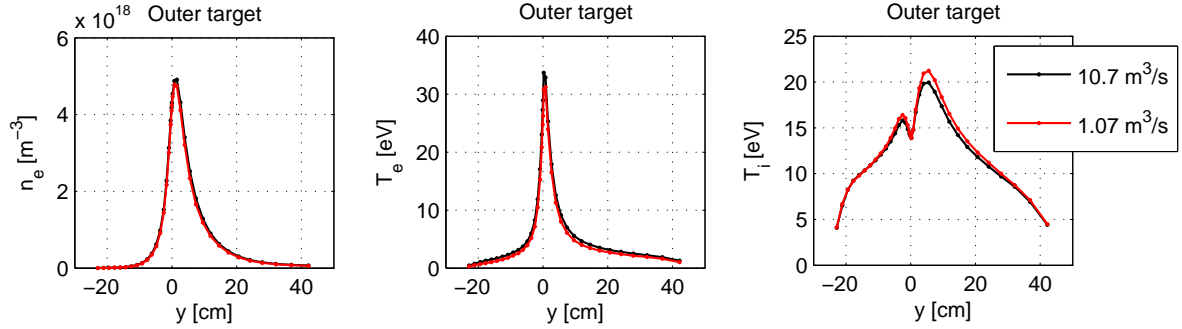


Figure 22. Radial profiles of the density and temperature at the outer target in the simulation with different pumping speed.

Comments on separatrix location in the discharge 30356

As a rough guide for the separatrix position, T_e at the separatrix can be estimated from a simple analytic model [22], in our case as $T_e \approx (7P_{\text{inp}}L_{\parallel}B/8\kappa_0\pi R\lambda_Q B_{\text{pol}})^{2/7} \approx 40$ eV, or 32 eV if a uniform source is assumed instead of a localized one. This would suggest an outward shift of the TS profiles in Figs. 2 and 3, as the original experimental data for the discharge 30356 show an average value around 25 eV. Such shift is consistent with Fig. 5.

Alternatively, the two-point model [22] is often used to estimate the separatrix location. It should be noted that using the simple pressure balance as described by the two-point model appears to be inaccurate in our case according to the SOLPS simulation

where more general equations than the two-point model are used. The simulation result shows that $2n_e^t T_e^t / n_e^u T_e^u \neq 1$ (t denotes target values and u upstream values), see Fig. 23. Also notice a large change in the target/upstream pressure ratio p_t/p_u when the ion temperature is taken into account, as a result of $T_i > T_e$ in the simulation.

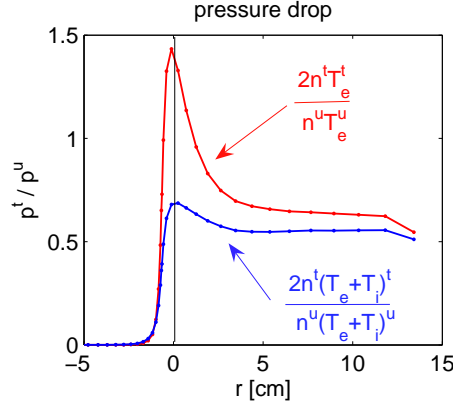


Figure 23. The ratio of the target and upstream pressure in the simulation calculated from expressions shown in the graph – (i) assuming $T_i = T_e$, (ii) allowing $T_i \neq T_e$.

References

- [1] Morris W et al 2014 *IEEE Trans. Plasma Sci.* **42** 402
- [2] Fishpool G et al 2013 *J. Nucl. Mater.* **438** S356
- [3] Kotschenreuther M et al 2010 *Nucl. Fusion* **50** 035003
- [4] Stangeby P C *Modified Two Point Model of the SOL to allow for variation in R_{target}* , http://starfire.utoronto.ca/divimp/publications/2PM-with-R_t-variation-10Aug11-inc.pdf
- [5] Valanju P M et al 2009 *Phys. Plasmas* **16** 056110
- [6] Schneider R et al 2006 *Contrib. Plasma Phys.* **46** 3
- [7] Havlíčková E et al 2014 *Plasma Phys. Control. Fusion* **56** 075008
- [8] Havlíčková E et al 2014 *Contrib. Plasma Phys.* **54** 448
- [9] Havlíčková E et al *J. Nucl. Mater.* (submitted)
- [10] Havlíčková E et al (to be submitted)
- [11] Reimold F et al *21st International Conference on Plasma Surface Interactions*, Kanazawa, Japan, 2014, I17
- [12] Aho-Mantila L et al 2012 *Nucl. Fusion* **52** 103006
- [13] Huang J et al 2010 *Plasma Phys. Control. Fusion* **52** 075012
- [14] Kirk A et al 2004 *Plasma Phys. Control. Fusion* **46** 1591
- [15] Rozhansky V et al 2012 *Nucl. Fusion* **52** 103017
- [16] Harrison J et al 2013 *J. Nucl. Mater.* **438** S375
- [17] Pitcher C S et al 1997 *J. Nucl. Mater.* **241-243** 696
- [18] Lipschultz B et al 1997 *J. Nucl. Mater.* **241-243** 771
- [19] Thornton A et al 2014 *Plasma Phys. Control. Fusion* **56** 055008
- [20] Field A private communications
- [21] Tskhakaya D private communications
- [22] Stangeby P C 2000 *The plasma boundary of magnetic fusion devices* (Bristol: IOP Publishing)